Available online at www.sciencedirect.com

ScienceDirect

Geochimica et Cosmochimica Acta 284 (2020) 107–119

Geochimica et Cosmochimica Acta

www.elsevier.com/locate/gca

Arsenic sequestration in pyrite and greigite in the buried peat of As-contaminated aquifers

H.Y. Wang [a,*], J.M. Byrne [b], J.P.H. Perez [c,d], A.N. Thomas [a], J. Göttlicher [e], H.E. Höfer [f], S. Mayanna [c], A. Kontny [a], A. Kappler [b], H.M. Guo [g], L.G. Benning [c,d], S. Norra [a]

[a] *Institute of Applied Geoscience, Working Group of Environmental Mineralogy and Environmental System Analysis, Karlsruhe Institute of Technology (KIT), 76131 Karlsruhe, Germany*

[b] *Geomicrobiology, Center for Applied Geosciences, University of Tuebingen, 72074 Tuebingen, Germany*

[c] *GFZ German Research Center for Geoscience, 14473 Potsdam, Germany*

[d] *Department of Earth Sciences, Freie Universität Berlin, 12249 Berlin, Germany*

[e] *Institute of Synchrotron Radiation, Karlsruhe Institute of Technology (KIT), 76131 Karlsruhe, Germany*

[f] *Institute of Geoscience, Goethe University, 60438 Frankfurt, Germany*

[g] *State key Laboratory of Biogeology and Environmental Geology, China University of Geoscience, 100083 Beijing, China*

Received 9 February 2020; accepted in revised form 15 June 2020; Available online 29 June 2020

Abstract

Detrital peat (organic carbon-enriched deposit) with high arsenic (As) content is widely distributed in sediments where groundwater As contamination exists. Iron sulfides often persist in these sediments under anoxic conditions. However, the mechanisms and pathways of formation of iron sulfides and its potential contribution in controlling As mobility are still poorly understood. In this study, we examined three As-contaminated peat sediments from the Hetao Basin in China to gain better understanding of the complex interplay between iron sulfides formation and As mobility. We employed high-resolution spectroscopic techniques, including X-ray absorption spectroscopy and ^{57}Fe Mössbauer spectroscopy, coupled with electron microscopy to determine the speciation of iron sulfides and the associated As in the peat sediments.

Pyrite (FeS_2) and metastable greigite (Fe_3S_4) persisted in peat as end-members of S and Fe diagenetic pathways. The Fe-rich phyllosilicates and decaying plant tissues provided the ideal micro-environments for pyrite and greigite nucleation. Pyrite formation most likely occurred via the polysulfides pathway in the surface water-sediments interface during early diagenetic process, while the relative enrichment of reactive Fe compared to sulfide possibly inhibited the transformation of greigite to pyrite in such Fe-rich sediments.

Our results revealed that the peat sediments could act as a stable sink for As immobilization under steady groundwater anoxic conditions, with As content up to 250 mg/kg and large proportions (40 to 60 wt.% As) sequestered in pyrite and greigite. Pyrite crystallites had up to 1 wt.% As content through the replacement of the S^{-I} sites. Greigite crystallites had a relatively constant As content ranging from ~500 to ~1400 mg/kg. Instead of being adsorbed or structurally incorporated, arsenic formed distinct arsenic sulfide phase in the greigite-enriched sediments, which was analogous to realgar. The transfer of As from iron sulfides to ferrihydrite temporarily retarded As release into groundwater under slightly oxic groundwater conditions. However, the reductive dissolution of ferrihydrite and potential subsequent As re-release could be a source of As in groundwater under disturbed redox conditions.

Keywords: Peat; Arsenic; Greigite; Pyrite; Sediment biogeochemistry; Early diagenesis

* Corresponding author.
E-mail address: hongyan.wang@kit.edu (H.Y. Wang).

https://doi.org/10.1016/j.gca.2020.06.021
0016-7037/

1. INTRODUCTION

Over a hundred million people are exposed to groundwater with high levels of arsenic (As) (>10 μg/L) globally, particularly in South and Southeast Asia including the Ganges-Brahmaputra-Megha, Red River and Mekong Deltas and the basins belong to the Yangtze and Yellow River catchments (Winkel et al., 2008; Fendorf et al., 2010; Wang et al., 2019b). It is widely accepted that microbial reduction of Fe (oxyhydr)oxides coupled to organic carbon oxidation causes the release of Fe (oxyhydr)oxides-bound As into groundwater (Nickson et al., 1998; Islam et al., 2004; Guo et al., 2013). The reactivity and availability of organic matter, partitioning of As in solids and the presence of other redox-active species (e.g., NO_3^-, SO_4^{2-}) largely influence As speciation and partitioning between groundwater and solid phases (O'Day et al., 2004b; Langner et al., 2012; Stuckey et al., 2015a; Zhu et al., 2017; Smith et al., 2017).

Peat is a heterogeneous mixture of (partly) decayed plant materials that accumulate anaerobically (Naafs et al., 2019). Abundant reactive organic matter provides electrons for the reductive transformation of Fe (oxyhydr)oxides, thereby influencing the behavior of trace elements that are bound onto Fe (oxyhydr)oxides such as As. In the As contaminated aquifers in South and Southeast of Asia, peat formed in Holocene epoch or the last glacial period is widely embedded in the sediments (McArthur et al., 2001; Wang et al., 2018, 2019b). Influence of the buried peat for As mobilization has been extensively discussed in terms of reductive dissolution of Fe(III) (oxyhydr)oxides. On one hand, dissolved organic matter degraded from plants in the peat lenses can be transported to different locations by groundwater flow, stimulate microbial reduction of Fe(III) (oxyhydr)oxides and As (V) reduction and thereby releasing arsenic into groundwater (McArthur et al., 2001, 2004; Anawar et al., 2003; Fendorf et al., 2010). On the other hand, the detrital peat buried in the sediments can serve as a special sink for As. Following the reductive dissolution of Fe(III) (oxyhydr) oxides and As(V) species, mobilized As(III) species can be subsequently sequestrated by sulfides, with sulfide arising from reduced organic sulfide in peat or microbial reduction of SO_4^{2-} (Stuckey et al., 2015b; Wang et al., 2018; Knappová et al., 2019). Furthermore, recent research shows that reactive organic thiol groups formed by incorporating inorganic sulfide into organic carbon can adsorb As in contaminated peatlands, providing another sink for As (Langner et al., 2012, 2013; Wang et al., 2018). Therefore, the influence of peat for As behavior is complex and affected by Fe-C-S coupled mineralization pathways. Understanding the diagenetic process in the peat layers and related As speciation are vital to gain better understanding on the influence of peat sediments in As immobilization in contaminated anoxic environments.

Arsenic-Fe sulfides associations are common features in peat layers, and act an important role for As immobilization. Iron sulfides found in the natural sediments mainly include mackinawite (nominally "FeS"), greigite and pyrite (Wilkin and Ford, 2006; Pickard et al., 2017; Knappová et al., 2019). Recent research suggests that Fe sulfides are main As carriers in the detrital peat of As contaminated aquifer in South and Southeast of Asia. For example, arsenic is mainly sequestrated in pyrite found in peat from Mekong River Delta and Bangladesh (Lowers et al., 2007; Stuckey et al., 2015b; Wang et al., 2018). Several studies have been conducted to study the mechanisms of Fe sulfides formation as well as the adsorption/incorporation behavior of As in the laboratory scale (Benning et al., 2000; Bostick and Fendorf, 2003; Blanchard et al., 2007; Kirk et al., 2010; Le et al., 2017). However, the diagenetic formation process in natural settings and adsorption/incorporation mechanisms for As are still not sufficiently understood because Fe sulfides and related As species are difficult to characterize and quantify due to its oxygen-sensitive nature and poorly crystalline properties.

Based on the assumption that diagenetic process especially Fe sulfides formation in the peat can influence As partitioning in sediments and groundwater, we separated three peat lenses from the sediments of Hetao Basin, an important inland basin draining Yellow river with As contaminated groundwater. Using these, we seek to (1) define the S and Fe diagenetic minerals in peat lenses, (2) investigate As speciation in both peat sediments and specific Fe sulfides, and (3) evaluate the potential role of peat layers in controlling the toxicity and mobility of As in aquifers. The buried peat in the Hetao Basin formed either by over-flowed flood debris or swamps is analogous to other peat formed in As contaminated aquifers in South and Southeast Asia, therefore the research results can be applicable to comparable subsurface environments.

2. MATERIAL AND METHODS

2.1. Field area

The Hetao Basin is a typical inland basin lying in the central part of Inner Mongolia (China) with the Lang Mountains in the North and the Yellow River in the South, covering an area of about 13,000 km^2. In the early time of late Pleistocene (~120 ka) epoch, the Yellow River began to flow through the Hetao paleolake. At the same time, the paleolake started to shrink due to the cooling climate (Jia et al., 2016). Salt marshes as well as oxbow lakes were generated as a result of paleolake shrinkage and frequent movement of the Yellow River channels (Cai et al., 2019), resulting in the accumulation of organic matter. The study site was located in the flat plain of northwestern Hetao Basin which was one of most As contaminated area. The stratigraphy of the late Pleistocene and the Holocene covered a depth around 150 m, whereas the Holocene sediments primarily included alluvial-fluvial sediments with thicknesses of ~10 m (Deng et al., 2009). Further detailed information about the study area such as hydrological conditions were outlined in a previous study (Zhang et al., 2020).

2.2. Sediments collection, bulk geochemistry composition and mineral phase analysis

Two multilevel wells, K1 (41°0′9.00″N, 106°57′59.20″E) and K2 (41°1′2.10″N, 106°57′24.50″E), were selected in the study area. The wells were drilled in October 2015 by the China University of Geosciences (Beijing) (CUGB) using a circulatory drilling method. After bringing the cores to the surface, they were split into 10 cm sections according to lithology and color variations observed visually, and then capped and placed into N_2-purged Mylar bags. More detailed information about well construction and sediments sampling information has been reported by Zhang et al. (2020). Groundwater samples from different depths (sampling length: 1 m) were collected after the wells were constructed and then analyzed at CUGB. The geochemical and mineralogical composition of the sediments were analyzed at the Karlsruhe Institute of Technology (KIT). Methods for the groundwater sampling, geochemical analysis, and determination of elemental and organic carbon content and isotopic composition are detailed in the supplementary information (Supplementary text 1). Methods for mineralogical characterization of magnetically separated minerals, and sequential extractions of Fe-bearing phases in the bulk sediments are shown in the supplementary information (Supplementary text 2 and Supplementary Table S1). The magnetic susceptibility measurements of the peat sediments are described in detail in Supplementary text 3.

2.3. ^{57}Fe Mössbauer analysis

A section of peat was separated from each intact core for Mössbauer analysis at the University of Tübingen. Inside the glovebox (pure nitrogen atmosphere), dried powders of peat samples were loaded into Plexiglas holders (area 1 cm^2), forming a thin disc. Samples were kept in airtight jars under anoxic conditions at −20 °C until measurement. Holders were inserted into a closed-cycle exchange gas cryostat (Janis cryogenics) under a backflow of He to minimize exposure to air. Spectra were collected at 20 K using a constant acceleration drive system (WissEL) in transmission mode with a ^{57}Co/Rh source. All spectra were calibrated against a 7-μm thick α-^{57}Fe foil that was measured at room temperature. Analysis was carried out using Recoil (University of Ottawa) and the Voigt Based Fitting (VBF) routine (Rancourt and Ping, 1991). The half width at half maximum (HWHM) was constrained to 0.13 mm/s during fitting.

2.4. Scanning Electron Microscopy (SEM) and Electron probe microanalysis (EPMA)

Thin sections for SEM imaging and EPMA analysis were prepared at KIT. A section of peat was separated from intact cores, and embedded in an arsenic free-resin in the glovebox after drying. Sections of 1-mm thickness were cut and polished down to a thickness of 80 μm. Thin sections were stored in the glovebox until analysis.

Carbon-coated thin sections were used for SEM imaging and EPMA analysis. SEM images were acquired at the GFZ German Research Center for Geosciences using a Zeiss Ultra Plus FE-SEM at an acceleration voltage of 3 kV with10 μm aperture distance using an In-lens secondary electron detector. Following mineral observations using SEM, selected particles and areas were analyzed at Goethe University by wavelength spectrometer electron probe microanalysis (EPMA, JEOL 8900). The operating conditions were 20 keV accelerating voltage and 20nA beam current. Iron, S, Si, Ca, Mg and As concentrations were quantified using peak counting times of 10 s for Fe, S, Si, Ca, Mg, and 60 s for As. The detection limit for As was about 90 mg/kg. For As, S and Fe mapping, pixel size was set to 0.1 μm × 0.1 μm. The analysis volume for particles was approximately 0.2–0.3 μm based on the Monte Carlo simulations.

2.5. As, S and Fe K-edge X-ray absorption spectroscopic analysis

The speciation and local bonding environment of As, S and Fe in selected peat samples were characterized using X-ray absorption spectroscopy (XAS) analysis at the SUL-X beamline at the ANKA synchrotron radiation facility (KIT). Samples were collected from each peat and ground into powder after drying in the glovebox. A sample mass for Fe K-edge XAS analysis was calculated by the program XAFSmass and mixed with boron nitride (Sigma-Aldrich) prior to analysis (Klementiev, 2012). For As and Fe K-edge XAS analysis, powdered samples were suspended in deoxygenated water in the glovebox, drop-casted onto Kapton tape, and sealed using a second piece of Kapton tape. Arsenic K-edge EXAFS spectra for sample K2-28 was analyzed at the BM23 beamline of the European Synchrotron Radiation Facility (ESRF, Grenoble, France) using the same sample preparation method. For S K-edge XAS measurements, dried peat samples were directly loaded onto the Kapton tape surface. Three scans to 12 scans were collected per sample for each As, Fe and S K-edge XAS spectrum. Data reduction and analysis of XAS spectra were performed using Athena software package (Ravel and Newville, 2005). Experimental and data analysis procedures can be found in the supplementary information (Supplementary text 4).

3. RESULTS

3.1. Geochemical composition of peat sediments

Surface sediments (~10 m) from cores K1 and K2 were yellowish to brownish in color and fine-grained with a silt/-clay like texture, whereas gray aquifer sediments with interbedded brown/gray clay lenses were found at a depth of ~10 m (K1) and ~14 m (K2) to 82 m (maximum sampled depth) (Fig. 1). In borehole K1, a ~5 cm thick black peat band located between 80.4 and 80.5 m (K1-71) was composed of a poorly sorted mixture of fine sand, clay and small amounts of medium sand. In borehole K2, a ~5 cm poorly sorted clay peat band was found at a depth

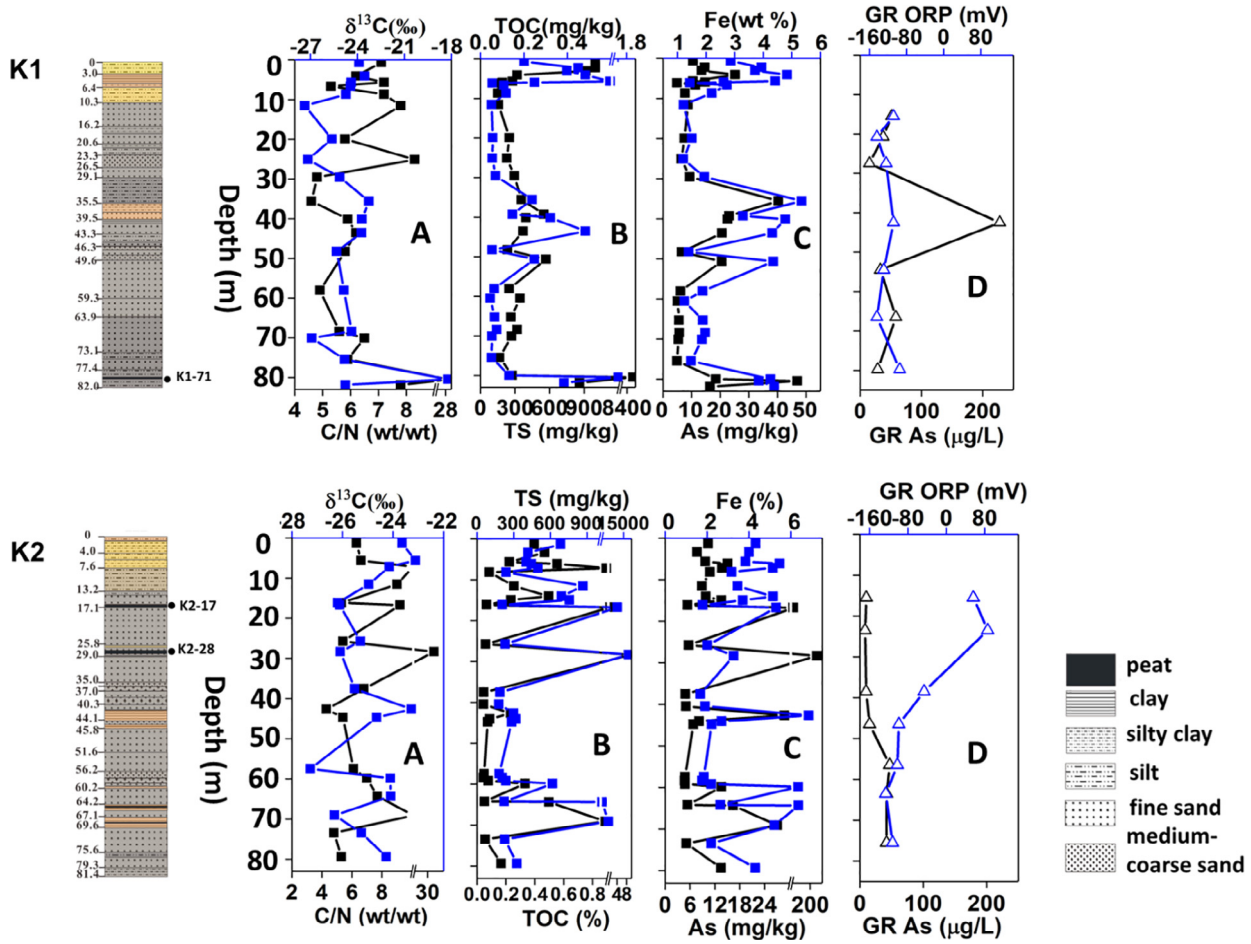

Fig. 1. Lithology and elemental content in the sediments profiles as well as groundwater redox conditions and As concentrations from different depths: (A) Isotope signature of organic carbon (δ^{13}Corg, blue) and ratio of organic carbon to total nitrogen (C/N, black); (B) total sulfur content (TS, blue) and total organic carbon (TOC, black); (C) total Fe (blue) and As content (black); and (D) groundwater redox conditions (GW ORP, blue) and As concentrations (black). Drawing color of the cores represents the visualized sediments colors, layers labeled with black dots (K1-71, K2-17, and K2-28) represent the analyzed peat sediments. (For interpretation of the references to colour in this figure legend, the reader is referred to the web version of this article.)

of 16.7–16.8 m (K2-17), and a peat layer composed of fine sand and visible detrital plant materials with thickness of at least of 10 cm was observed at a depth of 28.3–28.4 m (K2-28).

Arsenic content in the sediments was found to be between 4.7 mg/kg and 40.3 mg/kg (except for the peat layers) with generally higher content found in clay sediments (Table 1). Meanwhile, clay sediments had slightly higher Fe content (3.94% in average) than silt (2.86% in average) and sand (1.46% in average) (Table 1). Peat sediments showed significantly higher total organic carbon (TOC) and total sulfur (TS) content, and C/N ratios than in the underlying and overlying sediments (Fig. 1 and Table 1). Much higher As content was found in the peat lenses (up

Table 1
Geochemical compositions of studied peat sediments and comparison with other sediments.

Sample name	Depth(m)	As (mg/kg)	Fe (%)	TOC (%)	TS (mg/kg)	C_{org}/N ratio	δ^{13}Corg (‰)
K1-71	~80.4	46.9	3.85	1.70	8,836	29.1	−18.2
K2-17	~16.7	59.2	5.31	1.33	11,020	9.2	−26.1
K2-28	~28.3	256	3.27	9.52	155,970	31.6	−26.1
Clay/silty clay	–	18.6 ± 8.9	3.94 ± 0.72	0.40 ± 0.20	365 ± 156	5.9 ± 1.2	−23.7 ± 0.5
Silt	~	12.0 ± 5.1	2.86 ± 0.70	0.24 ± 0.14	376 ± 265	7.1 ± 2.4	−24.1 ± 0.5
Sand	~	6.0 ± 1.4	1.46 ± 0.26	0.06 ± 0.01	163 ± 67	6.2 ± 1.3	−25.7 ± 0.9

to ~250 mg/kg) in comparison with other sediments (Fig. 1 and Table 1). In comparison with peats K1-71 and K2-17, peat K2-28 had much higher organic matter as well as total S content (Table 1).

3.2. Fe-containing phases in the peat sediments

3.2.1. Fe K-edge XAS and ^{57}Fe Mössbauer analysis

The pre-edge inflection point near 7112 eV and primary inflection point near 7119 eV in the first derivative Fe K-edge XANES spectra suggested that Fe sulfides were abundant in the peat lenses (Supplementary Fig. S3) (O'Day et al., 2004a). The results of Fe K-edge extended X-ray absorption fine structure (EXAFS) linear combination fitting (LCF) revealed that, aside from phyllosilicates (~53% and ~66%), greigite (~23% and ~42%) was the primary Fe-bearing mineral phase in K2-17 and K1-71, respectively. Meanwhile, pyrite (~22%) and ferrihydrite (~17%) in combination with phyllosilicates (~59%) were the dominant Fe-bearing phases in K2-28 (Fig. 2 a and Table 2).

^{57}Fe Mössbauer spectroscopy was used to identify Fe-bearing mineral phases as a complementary technique to synchrotron-based Fe K-edge EXAFS (Fig. 2b). The parameters of the narrow sextet in the peat samples K2-17 and K1-71 were typical of greigite (magnetic hyperfine field of 31.2 T and 32.0 T, isomer shift: 0.59 and 0.57, quadrupole shift of 0.00 and −0.04) (Vandenberghe et al., 1992), comprising ~27% and ~30% of the Fe phases, respectively (Supplementary Table S6). Differences less than 10% in the greigite component between the Fe K-edge EXAFS and Mössbauer spectroscopy fits in peat sediments K2-17 and K1-71 is considered to be acceptable (Thomas-Arrigo et al., 2014; Chen et al., 2017).

Unfortunately, the similarity of phyllosilicates Fe(III) and pyritic Fe(II) in the Mössbauer spectra at 20 K can result to misidentification of pyrite in peat samples K2-17 and K2-28. However, the Fe K-edge EXAFS spectra of pyrite and phyllosilicates can be easily distinguished (O'Day et al., 2004a), and these fitting results matched the Mössbauer spectroscopy fits (Table 2 and Supplementary Table S6). Furthermore, an expected ferrihydrite sextet in the 20 K Mössbauer spectra was not observed, even in sample K2-28, while Fe (oxyhydr)oxides were detected by Fe K-edge EXAFS. The magnetic ordering temperature of ferrihydrite is strongly dependent on the mineral purity, crystallite size and crystallinity, and as such the absence of a ferrihydrite sextet in the Mössbauer spectra does not necessarily mean that it is absent, as shown using other spectroscopic measurements (Wang et al., 2016). The presence of ferrihydrite in the K2-28 peat sample was further confirmed by measurements of magnetic susceptibility, which decreased in value from −192 °C to 0 °C (Supplementary Fig. S2) (Pannalal et al., 2005).

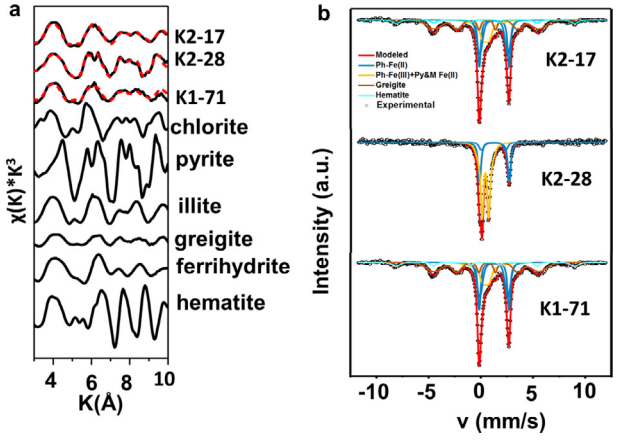

Fig. 2. (a) LCF fitting results of Fe K-edge EXAFS. Black lines represent experimental data for samples and model compound spectra used for fitting, and red dashed lines represent LCF fits. (b) ^{57}Fe Mössbauer spectra collected at 20 K for peat sediments, ph: phyllosilicates; py: pyrite; M: mackinawite.

3.2.2. Texture and morphologies of Fe-bearing phases (SEM-EDX analysis)

The Fe-bearing minerals texture and morphologies were evaluated according to SEM-EDX analysis based on the known minerals which were obtained by Fe K-edge XAS and Fe Mössbauer analysis.

Greigite aggregates nucleated in detrital silicates and decaying plant tissues, and less in gypsum/anhydrite (Fig. 3). The grain size ranged from ~80 nm to ~500 nm, whereas diverse crystallite habits were observed, including cuboidal, prismatic, and elongated particles. Neoformation of pyrite was also primarily occurred in confined spaces including plant tissues, phyllosilicates grains. The diameters of framboidal pyrites ranged from ~5 μm to ~40 μm (Fig. 3). Framboidal crystallites showed either octahedral, cubic (~2 μm in diameter) or spherical crystal habits (~1 μm in diameter). Massive pyrite crystals occurred with octahedral, cubic or irregular habits, with diameters up to ~10 μm. Ferrihydrite was found to be associated with pyrite particles.

3.3. Sulfur speciation in the peat sediments

Sulfur speciation in the peat sediments was analyzed by S K-edge XANES spectra. Based on the primary white line positions, the presence of reduced organosulfur species can be ruled out since they often have white line positions at >2472 eV (Manceau and Nagy, 2012). The primary inflection points at ~2469.1 eV and ~2471.1 eV in K2-17 and ~2469.1 eV in K1-71 revealed that inorganic sulfides were the primary sulfur-bearing phases, whereas the pronounced inflection points of ~2471.2 eV and ~2481.6 eV in peat sample K2-28 corresponded to inorganic sulfides and SO_4^{2-} from evaporites, respectively (Fig. 4). Iron monosulfide minerals (FeS) were not used in the XANES and XANES first derivative LCF fitting because their characteristic features were not observed in either Fe K-edge XAS analysis or sequential experiments (Fig. 2 a and Supplementary Table S2). Sulfur K-edge first derivative XANES LCF fitting showed that S^{2-} is the dominant S-bearing phase in K1-71 (~93%) and K2-17 (~70%). In sample K2-28, ~30% and ~60% of S was in the form of S^{-1} and zero-valent sulfur (S_0), respectively (Fig. 4 and Table 2).

Table 2
Summary of S, Fe and As K-edge XANES or EXAFS LCF fitting results.

Sample	Mineralogical composition (% mol S)				
	XANES first-derivative				
	Pyrite	Greigite	S_0	$CaSO_4 \cdot 2H_2O$	R^2
K2-17	14 (2.6)	70 (4.1)	15 (3)	1 (0.4)	0.091
K2-28	30 (2.0)	–	61 (2.9)	9 (0.4)	0.039
K1-71	–	93 (1.2)	5 (1.1)	2 (0.3)	0.058
Sample	**Mineralogical composition (% mol As)**				
	XANES first-derivative				
	Realgar	**Arsenopyrite**	**As (III)-Fh**	**As (V)-Fh**	**R^2**
K2-17	47 (6.9)	0 (4.2)	46 (2.1)	7 (1.5)	0.0245
K2-28	8(5.0)	61 (6)	3.8 (2.4)	27 (1.7)	0.0516
K1-71	41 (0.5)	–	50 (1.8)	10 (1.1)	0.0197
Sample	**Mineralogical composition (% mol Fe)**				
	EXAFS				
	Pyrite	**Greigite**	**Chlorite**	**Illite**	**Hematite**	**Ferrihydrite**	**R^2**
K2-17	3 (0.8)	23 (2.5)	19 (1.5)	47 (3.9)	8 (0.9)	–	0.0469
K2-28	23 (0.9)	–	39 (1.4)	18 (3.1)	-	21 (6.4)	0.0445
K1-71	–	42 (4.5)	24 (2.8)	29 (3.7)	5 (6.8)	–	0.1581

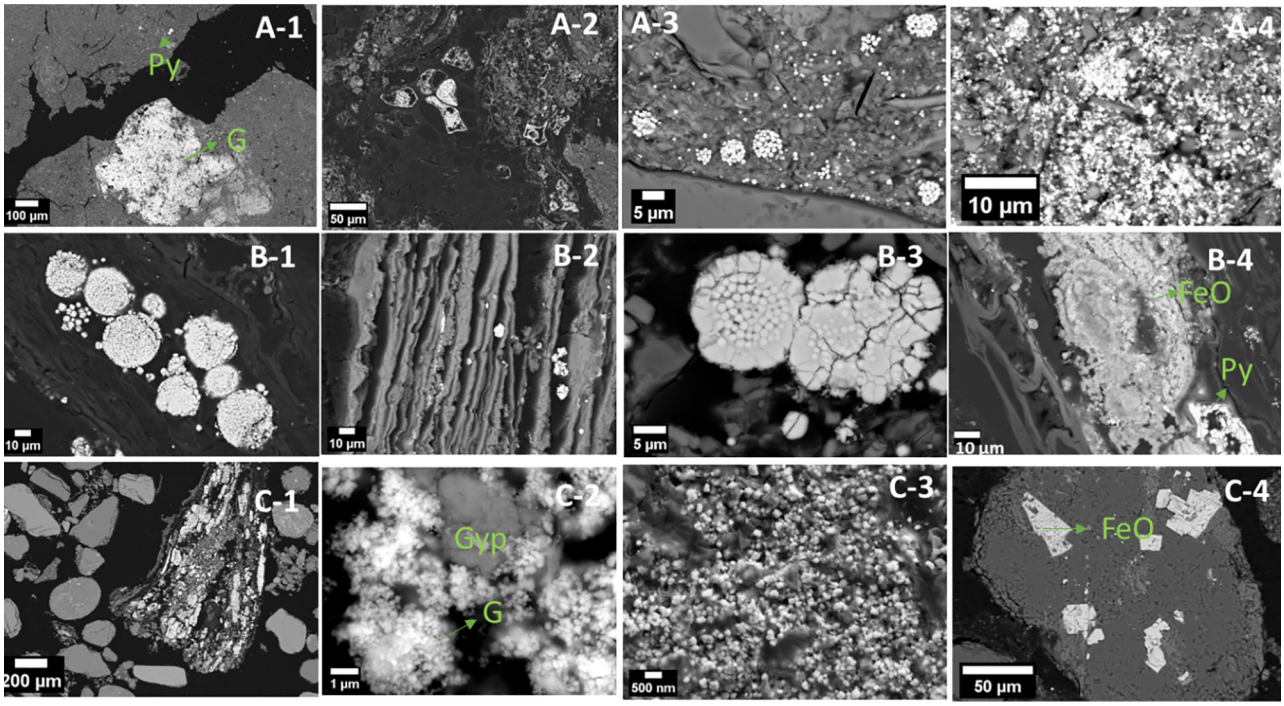

Fig. 3. Representative images of peat samples (A) K2-17, (B) K2-28 and (C) K1-71. (A-1) Representative greigite (G) and framboidal pyrite (Py) areas as indicated. (A-2) Greigite/pyrites nucleation in plant cells. (A-3) and (A-4) Nucleation of pyrites/greigite in phyllosilicates. (B-1) Framboidal and massive pyrites nucleation in plant tissues. (B-2) Massive pyrites nucleation in the phyllosilicates. (B-3) Framboidal pyrites nucleation in phyllosilicates. Overgrowth rims and interior crystallites were visible. (B-4) Mixture of ferrihydrite and pyrites in plant tissues/cells. (C-1) Greigite nucleation in phyllosilicates. (C-2) Greigite (G) nucleation in gypsum/anhydrite (Gyp). (C-3) Scattered electron images to show greigite grains. (C-4) Clastic iron oxides (FeO) in the sediment matrix.

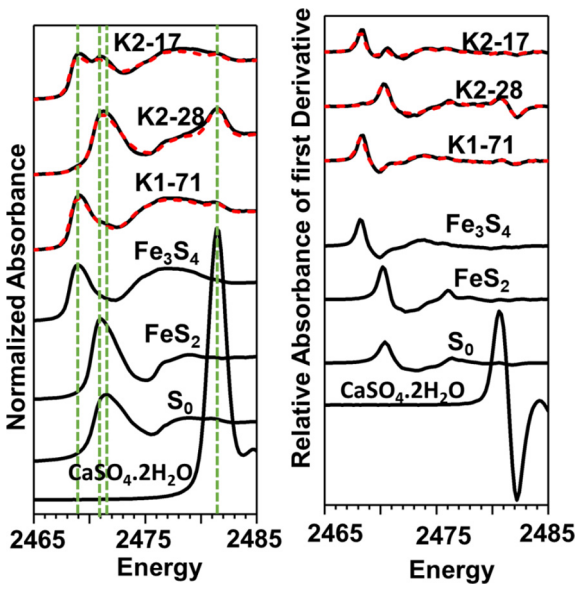

Fig. 4. Results of LCF fitting for S K-edge XANES and first derivative K-edge XANES spectra. Black lines represent experimental data, whereas red dashed lines represent the fits. Green dashed lines represent inflection points of selected model compounds. (For interpretation of the references to colour in this figure legend, the reader is referred to the web version of this article.)

3.4. Arsenic speciation and distribution in the peat sediments

3.4.1. As K-edge XAS analysis

The peat sediments of K1-71 and K2-17 both had white line energies near 11870 eV, which most likely indicates As (III) species were coordinated by sulfide (Smith et al., 2005). Arsenian pyrite/arsenopyrite detected in sample K2-17 do not seem to be major sinks for As due to the absence of the associated white line at ~11867.6 eV and the minimal pyrite content (<5%) (Fig. 5 A and Table 2). The first shells of the Fourier-transformed EXAFS spectra of K2-17 and K1-71 were comparable with the As(III)-O bond distance (~1.7 Å), while the second shell was consistent with the As(III)-S bond distance (~2.3 Å) (Bostick and Fendorf, 2003) (Fig. 5 D). First derivative K-edge XANES LCF fitting shows that ~40% of As is in the form of As-sulfide compounds in K2-17 and K1-71 while around 50% of As is in the form of arsenite (Table 2).

In peat K2-28, two inflection points occurred at ~11868 eV and ~11874 eV (Fig. 5 A), suggesting that the sample was mainly composed of arsenopyrite/arsenian pyrite (~11868 eV) and arsenate (~11874 eV). First derivative As K-edge XANES LCF fitting showed that ~61% and ~7% of As was presented as arsenopyrite/arsenian pyrite and As(V) species, respectively (Table 2).

3.4.2. Arsenic content and distribution in pyrite and greigite

Arsenic content of the pyrite and greigite grains was measured by EPMA and summarized in Table 3. Arsenic content in the pyrite grains ranged from <90 mg/kg (detection limit of EPMA) to ~11,000 mg/kg in both K2-17 and K2-28, respectively. Weak linear least squares fit was obtained for the As:S atomic ratio in the pyrite grains ($R^2 = 0.26$) (Fig. 6). Framboidal rims with over-grown pyrite crystallites contained more As than the framboid centers evidenced by two framboid measurements (Supplementary Table S5). Arsenic distributions in pyrites were heterogeneous, while the spatial distribution of As fluorescence intensities in the framboids showed a different picture compared to S and Fe (Fig. 7). Ferrihydrite aggregates had average As content about 4000 mg/kg, which was comparable with the average As content in pyrite measured using EPMA in peat K2-28 (Supplementary Table S5).

In contrast to pyrite, arsenic had a relatively homogeneous distribution in the greigite grains ranging from 500 to 1400 mg/kg (Table 3). Spatial As distribution was similar to the distribution of S and Fe fluorescence intensities (Fig. 7). Unfortunately, the result obtained from EPMA analysis may slightly underestimate the As content in the pyrite and greigite, while the total weight percent of S and Fe is 80% and 93% (on average) for greigite and pyrite, respectively (Supplementary Table S5). Except Fe (oxyhydr)oxides and sulfides, Fe-bearing phyllosilicates, especially clay minerals such as illite and chlorite, can also incorporate/adsorb As (Fakhreddine et al., 2015). However, our results showed that the influence from phyllosilicates was limited, as shown by the S/Fe atom ratios of pyrite and greigite which were similar to the stoichiometric ratios (Table 2). Furthermore, the distribution patterns of elements including Si, Mg and K, which are the main components of phyllosilicates, do not show any correlations with As distributions (Supplementary Fig. S4).

4. DISCUSSION

4.1. Diagenetic formation of Fe sulfides

The main minerals in the peat sediments include quartz, feldspar, carbonates and clay minerals, which has similar composition with the other sediments in the cores (Wang et al., 2019a). This suggests that the peat sediments have the same provenance with other sediments. Furthermore, the Fe sulfides found in the peat are likely of authigenic origin which can only be transported via small scales because they are susceptible to oxidation (Lowers et al., 2007). Therefore, the Fe sulfides found in the peat sediments were formed *in situ*.

Two proposed mechanisms, which are still under debate, can explain this pyrite formation via mackinawite (nominally "FeS") transformation, either by "FeS" reacting with polysulfides/elemental sulfur (S_0) (Eq. (1)) or "FeS" reacting with H_2S (Eq. (2)) (Benning et al., 2000):

$$FeS + S_0 \rightarrow FeS_2 \quad \text{or} \quad FeS + S_n^{2-} \rightarrow FeS_2 + S_{n-1}^{2-} \tag{1}$$

$$FeS + H_2S \rightarrow FeS_2 + H_2 \tag{2}$$

Reaction between S_0 precipitates and mackinawite [Eq. (1)] is most likely the dominant mechanism of pyrite formation since large proportions of S_0 (60% of total S) are detected together with pyrite. S_0 could have formed though sulfide oxidation coupled with Fe(III) reduction in such Fe-enriched sediments. Formation of pyrite via the polysulfides/S_0 pathway is typical in the oxic-anoxic transition

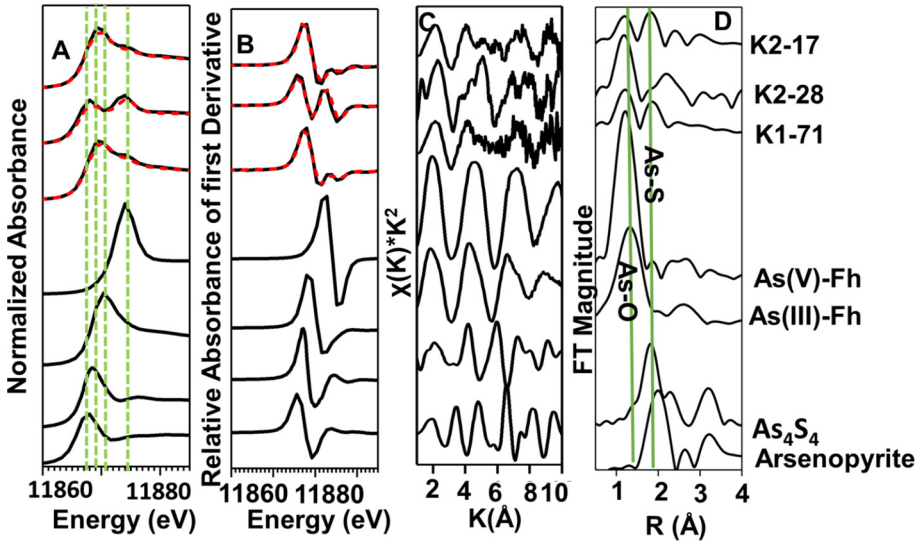

Fig. 5. As K-edge (A) XANES and (B) first-derivative XANES spectra of peat sediments and selected model compounds. The red dashed lines represent fits and the green dashed lines represent inflection points of selected model compounds (i.e., As(III)/As(V) adsorbed onto ferrihydrite, realgar (As_4S_4), arsenopyrite). (C) The k^2 weighted x(k) EXAFS spectra and their corresponding Fourier-transformations (D) The green lines represent the As-O and As-S bonding distances. (For interpretation of the references to colour in this figure legend, the reader is referred to the web version of this article.)

Table 3
Arsenic content in pyrite and greigite grains in the peat sediments based on the EPMA analyses.

Sample name	Mineral	S/Fe (avg. atomic %)	Min [As] (mg/kg)	Max [As] (mg/kg)	Average [As] ± SD (mg/kg)	n
K2-17	Pyrite	2.00	<90	11,040	5205 ± 5155	8
	Greigite	1.24	460	1380	1024 ± 341	5
K2-28	Pyrite	2.00	170	11,450	3760 ± 3,523	22
K1-71	Greigite	1.31	480	1270	895 ± 321	8

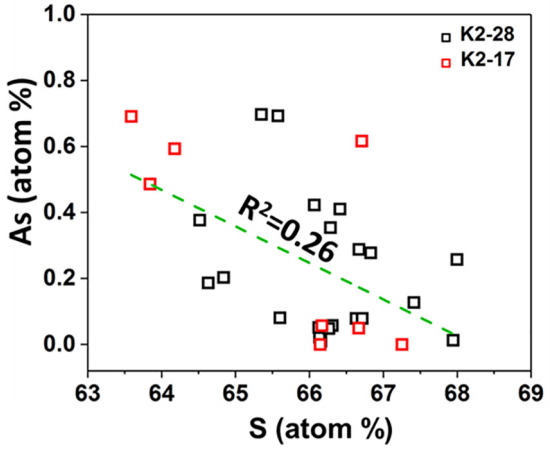

Fig. 6. Sulfur *vs* As atomic ratio measured by EPMA in peat samples.

zone of sediments (Berner, 1970; Neumann et al., 2005; Koeksoy et al., 2019), In the early diagenetic stage, the degradation of organic matter in the saturated water provides electrons for the reductive dissolution of SO_4^{2-} and Fe(III). This is followed by the subsequent precipitation of "FeS" upon saturation of Fe(II) and S(-II), and thereby resulting in the formation of pyrite via "FeS" reacting with S_0. The inhomogeneous framboid and euhedral pyrite sizes distribution could indicate unsteady geochemical conditions (Wilkin et al., 1996, 1997). The overgrowth of framboid, as well as the filled texture, is usually related to the secondary diagenetic growth of pyrite after formation in the surface water-sediment interface during early diagenetic process (Wilkin and Barnes, 1997), and the growth rate is limited by the sulfide supply, which can be constrained by labile organic matter in the sulfidic conditions or availability of SO_4^{2-} in porewater.

Greigite is a metastable iron sulfide mineral that is suggested to form as an intermediate during the oxidative transformation of mackinawite to pyrite (Vasiliev et al., 2008; Rickard and Luther, 2007; Pickard et al., 2017). However, the formation pathway and preservation mechanisms of this metastable mineral phase are still not fully understood, even though it has been increasingly recognized as an important sedimentary mineral. There have been few studies that show transformation of mackinawite to pyrite can be inhibited in natural sediments settings (Wilkin and Ford, 2006; Holmkvist et al., 2011; Burton et al., 2011). This is the case in one of the peats (K1-71) from Hetao Basin, wherein greigite is shown in the sample. In compar-

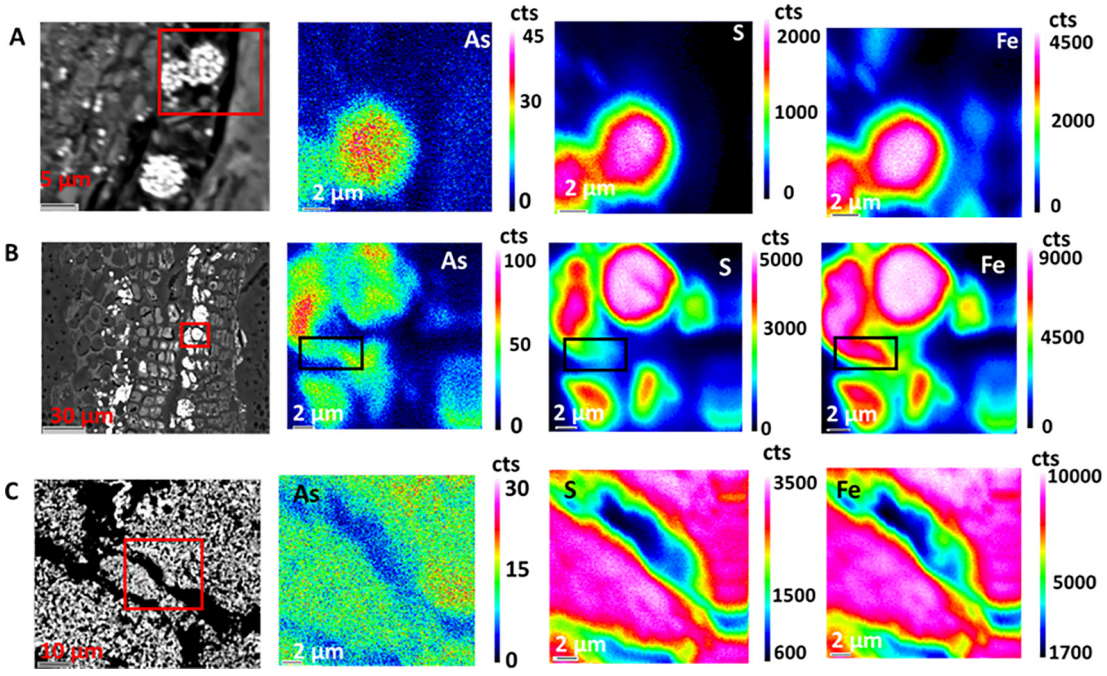

Fig. 7. Elemental mapping images of S, Fe and As elements obtained by EPMA, mapping area is indicated by red rectangle. (A) Map of framboidal pyrites area in sample K2-17. (B) Map of pyrites area in sample K2-28 which has nucleated in plant tissues, mapping area is indicated by a black rectangle corresponding to ferrihydrite (C) Map of greigite area in sample K1-71. (For interpretation of the references to colour in this figure legend, the reader is referred to the web version of this article.)

ison with pyrite-dominant peats, greigite-dominant peats have less organic matter and sulfur content, whereas the Fe content is comparable. This can be attributed to the likely precipitation of mackinawite which could remove sulfide from the pore water. The excess Fe^{2+} could exhaust sulfide, therefore, preventing polysulfide/S_0 formation and the subsequent transformation of greigite to pyrite. The lower sulfide flux in greigite-dominant layers compared to pyrite-dominant layers can be related to the limited labile organic carbon content or lower SO_4^{2-} concentration. This further emphasizes the importance of polysulfides/S_0 for the transformation of metastable iron sulfide precursors to pyrite under anoxic conditions in natural sediments. However, formation of greigite from a mackinawite precursor also requires an oxidant (Wilkin and Barnes, 1997; Schippers and JØrgensen, 2002; Hunger and Benning, 2007). In the surface water-sediments interface, penetration of oxidants such as O_2 and NO_3^- or metabolic activities of the SO_4^{2-} reducing bacteria probably favors the oxidation of FeS into greigite while polysulfides/S_0 is limited (Rickard, 1969; Picard et al., 2018; Mansor et al., 2019).

Phyllosilicates and decaying plant tissues provide the ideal micro-environments for pyrite/greigite nucleation and growth. Reactive Fe^{2+} provided by Fe-rich phyllosilicates via chemical or microbial reduction can induce supersaturation and precipitation of mackinawite on the silicates surface and subsequent transformation into pyrite/greigite. Some sulfate reducing bacteria such as *Desulfovibrio sp.* can reduce organic sulfur species into inorganic sulfides, which can also drive mackinawite formation in tissues (Altschuler et al., 1983). In addition, plant tissues can provide active surface area and decrease the oversaturation required for Fe sulfide nucleation (Rickard et al., 2007). Since organic sulfur is not detected in the S K-edge XANES spectra (<5%) of the peat samples, it suggests that microbial reduction of organic sulfur could have provided the inorganic sulfide needed for the formation of the mackinawite precursor. This result is contrary with previous study which has shown that inorganic sulfide is coupled with organic carbon as thiol functional groups, which in turn can sequester metalloids such as As (Langner et al., 2012; Wang et al., 2018). This might be a result of the differences in the ratio of reactive Fe to sulfur. The high abundance of reactive iron can remove inorganic sulfide in such Fe-rich sediments, thereby inhibiting transformation of inorganic sulfide to thiol functional groups.

4.2. Arsenic incorporation into Fe sulfides

Although relatively weakly correlated, the liner relationship between the S and As atomic ratios suggests that As possibly substitutes for S in the crystal structure of pyrite to form arsenian pyrite. The incorporation of As into pyrites is further evidenced by the As K-edge derivative XANES fits. In the pyrite-dominant peat sediments, our XANES data showed that approximate 60% of As exists as As(-I). The pyrite sequestration mechanism for As is consistent with previous studies of pyritic As sequestration mechanisms in natural sediments at low temperatures (Savage et al., 2000; Lowers et al., 2007). Arsenic content in the pyrite particles is between <90 mg/kg and 11,000 mg/kg with an average value around 5000 mg/kg,

showing that pyrite plays an important role for As sequestration in peat sediments. The similar maximum pyrite As concentrations in sediments from Bangladesh and the Hetao Basin suggests that the maximum As content incorporated into pyrite grains is around 1 wt.% under typical aquifer conditions (Lowers et al., 2007). The heterogeneous distributions of As in pyrite can be related to pyrite growth rates as well as contact time with porewater. The slightly higher As concentrations found in the framboid overgrowth rims as well as massive pyrites could be related to longer crystallization time, leading to enhanced As incorporation from the surrounding pore water into the pyrite structure (Lowers et al., 2007). Moreover, the resulting arsenian pyrites are still expected to be able to adsorb pore water As in the form of As(III) or As(V) species, or form As-S precipitates (Bostick and Fendorf, 2003; Qiu et al., 2018). This is consistent with our field observation that As concentration is relatively low in the groundwater with blackish-suspended particles, which likely corresponds to pyrite.

To our knowledge, adsorption and/or incorporation of As by greigite in both lab-scale batch reactions and in engineered and natural aquatic environments are still poorly investigated. The average As content of greigite particles as measured by EPMA, when multiplied by the amount of greigite determined in our samples, is comparable to the fraction of As bound in As sulfide (Supplementary text 5). Therefore, our results show that greigite is an important sink for As in the peat sediments with relatively lower S and organic carbon content and is primarily coordinated to sulfur within these particles, which is analogous to realgar evidenced by As K-edge XANES fitting. During greigite formation, oxidation of mackinawite coupled with As(III) species reduction may cause the surface precipitation of greigite and realgar. The findings in our study is consistent with the model predictions by Gallegos et al., (2008), where they argued that the formation of greigite is thermodynamically favorable by the reaction of As(III) species and mackinawite. Realgar and orpiment are also potential As carrier phases in the sulfidic sediments (O'Day et al., 2004a). However, greigite formation also uses up the available sulfide, therefore limiting As sulfides (i.e., realgar, orpiment) formation. Furthermore, it can also be constrained by relatively lower As concentrations in the pore water since As sulfide formation needs high porewater As concentration (O'Day et al., 2004b; Langner et al., 2012).

4.3. Significance of peat sediments for as mobilization process in aquifers

Our study clearly shows that Fe sulfides including greigite and pyrite formed in peat lenses could be important As sinks in contaminated aquifers. Sulfide flux controls Fe sulfides formation, while the sulfide flux would be in turn controlled either by labile organic matter in peat or SO_4^{2-} flux in the SO_4^{2-} limited groundwater (Lowers et al., 2007). In comparison to Fe (oxyhydr)oxides, greigite and pyrite are more thermodynamically stable under these sub-oxic conditions. Therefore, As release caused by reductive dissolution of iron (oxyhydr)oxides would not happen in the groundwater, and competitive adsorption between dissolved phosphate and silica and As on the reactive surfaces of Fe sulfides also cannot occur.

However, oxidation of arsenian pyrite to ferrihydrite-As (V) species can be ongoing process under slightly oxic conditions, as we have observed in the peat layer K2-28 (Fig. 1). Transferring As from surface or structure of arsenian pyrite onto ferrihydrite can temporarily retards the As release, which is supported by the similar average As content found in the ferrihydrite and pyrite as well as low As concentrations (<10 μg/L) in the groundwater (Fig. 1). However, ferrihydrite can potentially be reduced under disturbed groundwater redox conditions, which may cause elevated As concentration in the groundwater, since Fe sulfides re-formation is constrained by labile organic carbon. Groundwater redox conditions in draining delta or basins of South and Southeast Asia frequently experience anthropogenic perturbations, as well as seasonal fluctuations (Harvey et al., 2002; Fendorf et al., 2010), making Fe sulfides as an As source with respect to potential As remobilization. In recent years, *in situ* formation of Fe sulfides is suggested to remediate groundwater As pollution (Keimowitz et al., 2007; Pi et al., 2017). However, it is not suggested to apply it in such naturally unmanaged aquifer.

Previous studies also suggested that reactive organic carbon can be transported to other area by groundwater flow, therefore stimulating As release following by Fe (oxyhydr) oxides and As(V) species reduction (McArthur et al., 2001, 2004; Fendorf et al., 2010), but there is no solid evidence to prove that. Our study indicates that the labile organic matter buried in the peat sediments from aquifer can already be exhausted by early diagenetic Fe and S reduction. Our findings are consistent with the results found by Stuckey et al. (2015b), wherein organic matter leached from Mangrove deposits from Mekong delta cannot be able to simulate Fe (oxyhydr)oxides reduction.

5. SUMMARY AND CONCLUSION

Detrital peat formed from swamps or excessive flood debris is common in the As-contaminated aquifer of South and South-east Asia. To investigate the mineral diagenesis and sequestration behavior for As in these organic carbon-rich deposits, three peat lenses were retrieved from two cores with depths up to 80 m in the Hetao Basin.

Simultaneous microbial reduction of organic and inorganic sulfate favored Fe sulfide nucleation in the decaying plant tissues and phyllosilicates. Greigite and pyrite formed in surface water-sediment interface as the diagenetic minerals were stable in peat sediments under anoxic conditions. Excessive Fe(II) compared to sulfide due to lower sulfide flux potentially inhibited pyrite formation in the sulfidic porewater.

Peat sediments show a stable sink for As under steady anoxic conditions with As concentrations up to 250 mg/kg. Pyrite crystallites can have As content up to 11,000 mg/kg, with a majority of the As(-I) substitutes for

S(-I) in the pyrite structure. Arsenic content in the greigite grains is relatively homogeneous, ranging from ~500 to ~1400 mg/kg. We suggest that As forms distinct As sulfide precipitates in greigite-rich peats, as indicated by our As K-edge XAS data.

Anthropogenic perturbations and seasonal fluctuation of groundwater tables can largely change the groundwater redox conditions, for example, recharge of surface water caused by groundwater extraction infiltrates O_2 into groundwater. The increase of redox potential can induce Fe sulfides (e.g. pyrite and greigite) transfer to Fe (oxyhydr)oxides and temporarily retard As release into groundwater. However, reductive dissolution may in turn release As from the newly-formed iron (oxyhydr)oxide phase, as there is insufficient organic matter for transformation of these phases to Fe sulfide minerals and sequestration of As.

Declaration of Competing Interest

The authors declare that they have no known competing financial interests or personal relationships that could have appeared to influence the work reported in this paper.

ACKNOWLEDGEMENT

XRF, XRD, CSA, as well as HR-ICP-MS and IR-MS analysis were performed at KIT. The authors give thanks to Beate Oetzel, Claudia Moessner and Gesine Preuss for their technical assistance. We thank Ralf Steininger for his support during the collection of Fe, As and S K-edge XAS data at ANKA. The authors also acknowledge the CUGB group for their assistance during the field trip to the Hetao Basin and travel funding provided from the GRACE graduate program at KIT. We are also grateful for the advice from Elisabeth Eiche for C isotope analysis and Nicolas Börsig for XAS fitting analysis. The As K-edge XAS data of K2-28was collected at the BM23 beamline at ESRF (experiment no. EV-338), and the authors thank Sakura Pascarelli for assistance during beamtime. We further acknowledge the financial support from the Helmholtz Recruiting Initiative (award number I-044-16-01) awarded to L.G.B. J.P.H.P. and A.N.T. are supported by the European Union's Horizon 2020 Marie Skłodowska-Curie Innovative Training Network Grant No. 675219, and H.Y.W is supported by Chinese scholarship Council Grant No. 201606400055. Finally, we are grateful for the insightful comments from EIC Prof. Jeffrey Catalano, AE Prof. Caroline Peacock and three anonymous reviewers.

APPENDIX A. SUPPLEMENTARY MATERIAL

Supplementary data to this article can be found online at https://doi.org/10.1016/j.gca.2020.06.021.

REFERENCES

Altschuler Z. S., Schnepfe M. M., Silber C. C. and Simon F. O. (1983) Sulfur diagenesis in Everglades peat and origin of pyrite in coal. *Science* **221**(4607), 221–227.

Anawar H. M., Akai J., Komaki K., Terao H., Yoshioka T., Ishizuka T., Safiullah S. and Kato K. (2003) Geochemical occurrence of arsenic in groundwater of Bangladesh: sources and mobilization processes. *J. Geochem. Explor.* **77**(2–3), 109–131.

Benning L. G., Wilkin R. T. and Barnes H. L. (2000) Reaction pathways in the Fe–S system below 100 °C. *Chem. Geol.* **167**(1–2), 25–51.

Berner R. A. (1970) Sedimentary pyrite formation. *Am. J. Sci.* **268**(1), 1–23.

Blanchard M., Alfredsson M., Brodholt J., Wright K. and Catlow C. R. A. (2007) Arsenic incorporation into FeS2 pyrite and its influence on dissolution: a DFT study. *Geochim. Cosmochim. Acta* **71**(3), 624–630.

Bostick B. C. and Fendorf S. (2003) Arsenite sorption on troilite (FeS) and pyrite (FeS2). *Geochim. Cosmochim. Acta* **67**(5), 909–921.

Burton E. D., Johnston S. G. and Bush R. T. (2011) Microbial sulfidogenesis in ferrihydrite-rich environments: Effects on iron mineralogy and arsenic mobility. *Geochim. Cosmochim. Acta* **75**(11), 3072–3087.

Cai M., Ye P., Yang X. and Li C. (2019) Vegetation and climate change in the Hetao Basin (Northern China) during the last interglacial-glacial cycle. *J. Asian. Earth. Sci.* **171**, 1–8.

Chen C., Kukkadapu R. K., Lazareva O. and Sparks D. L. (2017) Solid-phase Fe speciation along the vertical redox gradients in floodplains using XAS and Mössbauer spectroscopies. *Environ. Sci. Technol.* **51**(14), 7903–7912.

Deng Y., Wang Y. and Ma T. (2009) Isotope and minor element geochemistry of high arsenic groundwater from Hangjinhouqi, the Hetao Plain, Inner Mongolia. *Appl. Geochem.* **24**(4), 587–599.

Fakhreddine S., Dittmar J. and Phipps D., et al. (2015) Geochemical triggers of arsenic mobilization during managed aquifer recharge. *Environ. Sci. Technol.* **49**(13), 7802–7809.

Fendorf S., Michael H. A. and van Geen A. (2010) Spatial and temporal variations of groundwater arsenic in South and Southeast Asia. *Science* **328**(5982), 1123–1127.

Gallegos T. J., Han Y. S. and Hayes K. F. (2008) Model predictions of realgar precipitation by reaction of As (III) with synthetic mackinawite under anoxic conditions. *Environ. Sci. Technol.* **42**(24), 9338–9343.

Guo H., Liu C., Lu H., Wanty R. B., Wang J. and Zhou Y. (2013) Pathways of coupled arsenic and iron cycling in high arsenic groundwater of the Hetao basin, Inner Mongolia, China: An iron isotope approach. *Geochim. Cosmochim. Acta* **112**, 130–145.

Harvey C. F., Swartz C. H., Badruzzaman A. B. M., Keon-Blute N., Yu W., Ali M. A., Jay J., Beckie R., Niedan V., Brabander D., Oates P. M., Ashfaque K. N., Islam S., Hemond H. F. and Ahmed M. F. (2002) Arsenic mobility and groundwater extraction in Bangladesh. *Science* **298**(5598), 1602–1606.

Holmkvist L., Ferdelman T. G. and Jorgensen B. B. (2011) A cryptic sulfur cycle driven by iron in the methane zone of marine sediment (Aarhus Bay, Denmark). *Geochim. Cosmochim. Acta*, 3581–3599.

Hunger S. and Benning L. G. (2007) Greigite: a true intermediate on the polysulfide pathway to pyrite. *Geochem. Trans.* **8**(1), 1.

Islam F. S., Gault A. G., Boothman C., Polya D. A., Charnock J. M., Chatterjee D. and Lloyd J. R. (2004) Role of metal-reducing bacteria in arsenic release from Bengal delta sediments. *Nature* **430**(6995), 68.

Jia L., Zhang X., Ye P., Zhao X., He Z., He X., Zhou Q., Li J., Ye M., Wang Z. and Meng J. (2016) Development of the alluvial and lacustrine terraces on the northern margin of the Hetao Basin, Inner Mongolia, China: Implications for the evolution of the Yellow River in the Hetao area since the late Pleistocene. *Geomorphol* **263**, 87–98.

Keimowitz A. R., Mailloux B. J., Cole P., Stute M., Simpson H. J. and Chillrud S. N. (2007) Laboratory investigations of enhanced sulfate reduction as a groundwater arsenic remediation strategy. *Environ. Sci. Technol.* **41**(19), 6718–6724.

Kirk M. F., Roden E. E., Crossey L. J., Brealey A. J. and Spilde M. N. (2010) Experimental analysis of arsenic precipitation during microbial sulfate and iron reduction in model aquifer sediment reactors. *Geochim. Cosmochim. Acta* **74**(9), 2538–2555.

Klementiev, K.V., 2012. XAFSmass. A program for calculating the mass of XAFS samples.

Knappová M., Drahota P., Falteisek L., Culka A., Penížek V., Trubač J., Mihaljevič M. and Matoušek T. (2019) Microbial sulfidogenesis of arsenic in naturally contaminated wetland soil. *Geochim. Cosmochim. Acta* **267**, 33–50.

Koeksoy E., Sundman A., Byrne J. M., Lohmayer R., Planer-Friedrich B., Halevy I., Konhauser K. O. and Kappler A. (2019) Formation of green rust and elemental sulfur in an analogue for oxygenated ferro-euxinic transition zones of Precambrian oceans. *Geology* **47**(3), 211–214.

Langner P., Mikutta C. and Kretzschmar R. (2012) Arsenic sequestration by organic sulphur in peat. *Nat. Geosci.* **5**(1), 66.

Langner P., Mikutta C., Suess E., Marcus M. A. and Kretzschmar R. (2013) Spatial distribution and speciation of arsenic in peat studied with microfocused X-ray fluorescence spectrometry and X-ray absorption spectroscopy. *Environ. Sci. Technol.* **47**(17), 9706–9714.

Le P. P., Blanchard M., Brest J., Boulliard J. C., Ikogou M., Stetten L., Wang S., Landort G. and Morin G. (2017) Arsenic incorporation in pyrite at ambient temperature at both tetrahedral SI and octahedral FeII sites: evidence from EXAFS-DFT analysis. *Environ. Sci. Technol.* **51**(1), 150–158.

Lowers H. A., Breit G. N., Foster A. L., Whitney J., Yount J., Uddin M. N. and Muneem A. A. (2007) Arsenic incorporation into authigenic pyrite, Bengal Basin sediment, Bangladesh. *Geochim. Cosmochim. Acta* **71**(11), 2699–2717.

Manceau A. and Nagy K. L. (2012) Quantitative analysis of sulfur functional groups in natural organic matter by XANES spectroscopy. *Geochim. Cosmochim. Acta* **99**, 206–223.

McArthur J. M., Banerjee D. M., Hudson-Edwards K. A., Mishra R., Purohit R., Ravenscroft P., Cronin A., Howarth R. J., Chatterjee A., Talukder T., Lowry D., Houghton S. and Chadha D. K. (2004) Natural organic matter in sedimentary basins and its relation to arsenic in anoxic ground water: the example of West Bengal and its worldwide implications. *Appl. Geochem.* **19**(8), 1255–1293.

McArthur J. M., Ravenscroft P., Safiulla S. and Thirlwall M. F. (2001) Arsenic in groundwater: testing pollution mechanisms for sedimentary aquifers in Bangladesh. *Water Resour. Res.* **37**(1), 109–117.

Mansor M., Berti D., Hochella M. F., Murayama M. and Xu J. (2019) Phase, morphology, elemental composition, and formation mechanisms of biogenic and abiogenic Fe-Cu-sulfide nanoparticles: a comparative study on their occurrences under anoxic conditions. *Am. Min.* **104**(5), 703–717.

Naafs B. D. A., Inglis G. N., Blewett J., McClymont E. L., Lauretano V., Xie S., Evershed R. P. and Pancost R. D. (2019) The potential of biomarker proxies to trace climate, vegetation, and biogeochemical processes in peat: a review. *Glob Planet Change* **179**, 57–79.

Neumann T., Rausch N., Leipe T., Dellwig O., Berner Z. and Böttcher M. E. (2005) Intense pyrite formation under low-sulfate conditions in the Achterwasser lagoon, SW Baltic Sea. *Geochim. Cosmochim. Acta* **69**(14), 3619–3630.

Nickson R., McArthur J., Burgess W., Ahmed K. M., Ravenscroft P. and Rahmanñ M. (1998) Arsenic poisoning of Bangladesh groundwater. *Nature* **395**(6700), 338.

O'Day P. A., Rivera, Jr, N., Root R. and Carroll S. A. (2004a) a) X-ray absorption spectroscopic study of Fe reference compounds for the analysis of natural sediments. *Am. Mineral.* **89**(4), 572–585.

O'Day P. A., Vlassopoulos D., Root R. and Rivera N. (2004b) b) The influence of sulfur and iron on dissolved arsenic concentrations in the shallow subsurface under changing redox conditions. *Proc. Natl. Acad. Sci.* **101**(38), 13703–13708.

Pannalal S. J., Crowe S. A., Cioppa M. T., Symons D. T., Sturm A. and Fowle D. A. (2005) Room-temperature magnetic properties of ferrihydrite: a potential magnetic remanence carrier? *Earth Planet. Sci. Lett.* **236**(3–4), 856–870.

Pi K., Wang Y., Xie X., Ma T., Liu Y., Su C., Zhu Y. and Wang Z. (2017) Remediation of arsenic-contaminated groundwater by in-situ stimulating biogenic precipitation of iron sulfides. *Water Res.* **109**, 337–346.

Picard A., Gartman A., Clarke D. R. and Girguis P. R. (2018) Sulfate-reducing bacteria influence the nucleation and growth of mackinawite and greigite. *Geochim. Cosmochim. Acta* **220**, 367–384.

Pickard D., Mussmann M. and Steadman J. A. (2017) Sedimentary sulfides. *Elements* **13**(2), 117–122.

Qiu G., Gao T., Hong J., Luo Y., Liu L., Tan W. and Liu F. (2018) Mechanisms of interaction between arsenian pyrite and aqueous arsenite under anoxic and oxic conditions. *Geochim. Cosmochim. Acta* **228**, 205–219.

Rancourt D. G. and Ping J. Y. (1991) Voigt-based methods for arbitrary-shape static hyperfine parameter distributions in Mössbauer spectroscopy. *Nucl. Instrum. Methods Phys. Res.: Beam Interact. Mater. Atoms* **58**(1), 85–97.

Ravel B. and Newville M. (2005) ATHENA, ARTEMIS, HEPHAESTUS: data analysis for X-ray absorption spectroscopy using IFEFFIT. *J. Synchrotron Radiat.* **12**(4), 537–541.

Rickard D. T. (1969) The microbiological formation of iron sulfides. *Stockholm Contrib. Geol.* **20**, 49–66.

Rickard D. and Luther G. W. (2007) Chemistry of iron sulfides. *Chem. Rev.* **107**(2), 514–562.

Rickard D., Grimes S., Butler I., Oldroyd A. and Davies K. L. (2007) Botanical constraints on pyrite formation. *Chem. Geol.* **236**(3–4), 228–246.

Savage K. S., Tingle T. N., O'Day P. A., Waychunas G. A. and Bird D. K. (2000) Arsenic speciation in pyrite and secondary weathering phases, Mother Lode gold district, Tuolumne County, California. *Appl. Geochem.* **15**(8), 1219–1244.

Schippers A. and Jørgensen B. B. (2002) Biogeochemistry of pyrite and iron sulfide oxidation in marine sediments. *Geochim. Cosmochim. Acta* **66**(1), 85–92.

Smith P. G., Koch I., Gordon R. A., Mandoli D. F., Chapman B. D. and Reimer K. J. (2005) X-ray absorption near-edge structure analysis of arsenic species for application to biological environmental samples. *Environ. Sci. Technol.* **39**(1), 248–254.

Smith R. L., Kent D. B., Repert D. A. and Böhlke J. K. (2017) Anoxic nitrate reduction coupled with iron oxidation and attenuation of dissolved arsenic and phosphate in a sand and gravel aquifer. *Geochim. Cosmochim. Acta* **196**, 102–120.

Stuckey J. W., Schaefer M. V., Benner S. G. and Fendorf S. (2015a) Reactivity and speciation of mineral-associated arsenic in seasonal and permanent wetlands of the Mekong Delta. *Geochim. Cosmochim. Acta* **171**, 143–155.

Stuckey J. W., Schaefer M. V., Kocar B. D., Dittmar J., Pacheco J. L., Benner S. G. and Fendorf S. (2015b) Peat formation concentrates arsenic within sediment deposits of the Mekong Delta. *Geochim. Cosmochim. Acta* **149**, 190–205.

Thomas-Arrigo L. K., Mikutta C., Byrne J., Barmettler K., Kappler A. and Kretzschmar R. (2014) Iron and arsenic

speciation and distribution in organic flocs from streambeds of an arsenic-enriched peatland. *Environ. Sci. Technol.* **48**(22), 13218–13228.

Vandenberghe R. E., De Grave E., De Bakker P. M. A., Krs M. and Hus J. J. (1992) Mössbauer effect study of natural greigite. *Hyperfine Interact.* **68**(1–4), 319–322.

Vasiliev I., Franke C., Meeldijk J. D., Dekkers M. J., Langereis C. G. and Krijgsman W. (2008) Putative greigite magnetofossils from the Pliocene epoch. *Nat. Geosci.* **1**(11), 782.

Wang H. Y., Guo H. M., Xiu W., Bauer J., Sun G. X., Tang X. H. and Norra S. (2019a) Indications that weathering of evaporite minerals affects groundwater salinity and As mobilization in aquifers of the northwestern Hetao Basin, China. *Appl. Geochem.* **109** 104416.

Wang X., Zhu M., Koopal L. K., Li W., Xu W., Liu F., Zhang J., Liu Q., Feng X. and Sparks D. L. (2016) Effects of crystallite size on the structure and magnetism of ferrihydrite. *Environ. Sci.: Nano.* **3**(1), 190–202.

Wang Y., Le Pape P., Morin G., Asta M. P., King G., Bártová B., Suvorova E., Frutschi M., lkogou M., Cong Pham V. H., Le Vo P., Herman, Charlet F. and Bernier-Latmani L. B. (2018) Arsenic speciation in Mekong Delta sediments depends on their depositional environment. *Environ. Sci. Technol.* **52**(6), 3431–3439.

Wang Y., Pi K., Fendorf S., Deng Y. and Xie X. (2019b) Sedimentogenesis and hydrobiogeochemistry of high arsenic Late Pleistocene-Holocene aquifer systems. *Earth-Sci. Rev.* **189**, 79–98.

Wilkin R. T., Arthur M. A. and Dean W. E. (1997) History of water-column anoxia in the Black Sea indicated by pyrite framboid size distributions. *Earth Planet. Sci. Lett.* **148**(3–4), 517–525.

Wilkin R. T., Barnes H. L. and Brantley S. L. (1996) The size distribution of framboidal pyrite in modern sediments: an indicator of redox conditions. *Geochim. Cosmochim. Acta* **60** (20), 3897–3912.

Wilkin R. T. and Ford R. G. (2006) Arsenic solid-phase partitioning in reducing sediments of a contaminated wetland. *Chem. Geol.* **228**(1–3), 156–174.

Wilkin R. T. and Barnes H. L. (1997) Formation processes of framboidal pyrite. *Geochim. Cosmochim. Acta* **61**(2), 323–339.

Winkel L., Berg M., Amini M., Hug S. J. and Johnson C. A. (2008) Predicting groundwater arsenic contamination in Southeast Asia from surface parameters. *Nat. Geosci.* **1**(8), 536.

Zhang Z., Guo H. M., Liu S., Weng H. C., Han S. B. and Gao Z. P. (2020) Mechanisms of groundwater arsenic variations induced by extraction in the western Hetao Basin, Inner Mongolia, China. *J. Hydrol.* **583**(124599), 1–13.

Zhu Y. G., Xue X. M., Kappler A., Rosen B. P. and Meharg A. A. (2017) Linking genes to microbial biogeochemical cycling: lessons from arsenic. *Environ. Sci. Technol.* **51**(13), 7326–7339.

Associate editor: Caroline L. Peacock